PAPER

Synergistic effects of hydrophobicity and gas barrier properties on the anticorrosion property of PMMA nanocomposite coatings embedded with graphene nanosheets†

Kung-Chin Chang,[a] Wei-Fu Ji,[a] Mei-Chun Lai,[a] You-Rong Hsiao,[a] Chien-Hua Hsu,[a] Tsao-Li Chuang,[b] Yen Wei,[c] Jui-Ming Yeh*[a] and Wei-Ren Liu*[d]

In this paper, the surface of a PMMA/graphene nanocomposite (PGN) with biomimetic hydrophobic structures was first prepared by the nanocasting technique and applied in corrosion protection coatings. First of all, a transparent soft template with negative patterns of a *Xanthosoma sagittifolium* leaf can be fabricated by thermal curing of the polydimethylsiloxane (PDMS) pre-polymer in molds at 60 °C for 4 h, followed by detaching the PDMS template from the surface of the natural leaf. Subsequently, PGN with a hydrophobic surface (HPGN) of the biomimetic natural leaf was fabricated, using PDMS as the negative template, through casting onto a cold rolled steel (CRS) electrode. The surface morphology of as-synthesized hydrophobic PMMA (HP) and PGN coatings was found to show lots of micro-scaled mastoids, each decorated with many nano-scaled wrinkles, which were investigated systematically by scanning electron microscopy (SEM). The contact angle (CA) of a water droplet on the sample surface can be increased from ~80° for the PMMA surface to ~150° for HP and HPGN and the sliding angle (SA) decreased from ~60° to 5°. The morphological studies of the dispersion capability of graphene nanosheets (GNSs) in the polymer matrix can be carried out by observation under a transmission electron microscope (TEM). It should be noted that HPGN coating was found to reveal an advanced corrosion protection effect on the CRS electrode as compared to that of neat PMMA and HP coatings based on a series of electrochemical corrosion measurements in a 3.5 wt% NaCl electrolyte. The enhancement of corrosion protection of HPGN coatings on the CRS electrode could be interpreted by the following two possible reasons: (1) the hydrophobicity repelled the moisture and further reduced the water/corrosive media adsorption on the epoxy surface, preventing the underlying metals from corrosion attack, as evidenced by contact angle (wettability) measurements. (2) The well-dispersed GNSs embedded in the HPGN matrix could hinder corrosion due to their relatively higher aspect ratio than clay platelets, which further effectively enhance the oxygen barrier property of HPGN, as evidenced using a gas permeability analyzer (GPA).

1. Introduction

Corrosion protection plays a prominent role in the modern metallic finishing industry. Previous surveys have shown that

corrosion is a very costly problem and has a major impact on the economies of industrial nations. Therefore, many organic and polymeric coatings have been employed to protect metals against corrosion.

Superhydrophobic surfaces, characterized by a water contact angle (CA) higher than 150°, are attracting much interest because of their high water repellency and practical applications such as in the prevention of adhesion of snow to antennas and windows, self-cleaning traffic indicators, metal refining, and stain-resistant textiles.[1–5] Considerable interest has now been given to the use of superhydrophobic materials as protective coatings.[6–11] Briefly, superhydrophobic coatings are known to be very resistant to water absorption.[12] This antiwetting property is relevant to its prevention from corrosion attack.

[a]Department of Chemistry, Center for Nanotechnology and Institute of Biomedical Technology at Chung-Yuan Christian University (CYCU), Chung Li, Taiwan 32023, Republic of China. E-mail: juiming@cycu.edu.tw

[b]Master Program in Nanotechnology and Center for Nanotechnology at CYCU, Chung Li, Taiwan 32023, Republic of China

[c]Department of Chemistry and Key Lab of Organic Optoelectronic & Molecular Engineering of Ministry of Education, Tsinghua University, Beijing 100084, China

[d]Department of Chemical Engineering, CYCU, Chung Li, Taiwan 32023, Republic of China

Recently, polymer nanocomposites reinforced by graphene-based materials such as graphene nanoplatelets (GNPs), graphene nanosheets (GNSs), and graphene oxide (GO) have been synthesized successfully, which show excellent properties[13–19] due to their very high aspect ratio of ~500 (ref. 20) and unique electrical, thermal and mechanical properties. The lower density and higher aspect ratio of conductive graphene, as compared with that of nonconductive clay platelets, have led to their potential application as advanced gas barrier polymer nanocomposites.[21]

To the best of our knowledge, some studies have previously been carried out on using polymers in various applications such as fabricating hydrophobic/superhydrophobic surfaces.[22–28] Therefore, developing hydrophobic/superhydrophobic polymers has become an interesting subject in materials science. In addition, the use of polymer coating materials to study the anticorrosive properties of hydrophobic/superhydrophobic surfaces has rarely been reported to date.[10,11,29–33] However, graphene-based nanocomposite anticorrosion coatings with hydrophobic surface have also rarely been studied.[34,35]

In this study, we used a nanocasting technique to develop advanced PMMA/graphene nanocomposite (PGN) anticorrosion coatings in order to directly duplicate the surface features of fresh plant leaves such as *Xanthosoma sagittifolium* leaves. The imprint of the hydrophobic *Xanthosoma sagittifolium* leaf was transferred onto the nanocomposite surface so that the resulting nanocomposite exhibited hydrophobicity to prevent corrosion. The nanocomposite anticorrosion coatings developed in this study also provided a 2-fold protection for metals from corrosion. The first part is that the hydrophobicity repelled moisture and further reduced the water/corrosive media adsorption on the PMMA surface, preventing the underlying metals from corrosion attack. The second one is the dispersed GNSs in the PMMA matrix to increase the tortuosity of the diffusion pathway of O_2 molecules. The detailed anticorrosion performance of the developed HPGN coatings was evaluated by a series of electrochemical corrosion measurements. Corrosion protection studies were performed on sample-coated CRS immersed in a corrosive medium (3.5 wt% sodium chloride aqueous solution).

2. Experimental

2.1 Materials and measurements

A fresh and natural *Xanthosoma sagittifolium* leaf was taken and dust was cleaned with water before use. Methyl methacrylate (MMA; Aldrich, 99.0%) was doubly distilled prior to use. Photo-initiator α-benzyl-α-(dimethylamino)-4-morpholinobutyro-phenon (Aldrich, 97.0%) was used as received. The liquid components (Sylgard 184) of PDMS were supplied by Dow Corning Corporation. Graphene nanosheets (SFG44-GNS) prepared from SFG44 synthetic graphite powders (TIMCAL®) were used. All reagents were of reagent grade unless otherwise stated.

Fourier transform infrared (FTIR) spectra were recorded using an FTIR spectrometer (JASCO FT/IR-4100) operating at room temperature. The nanostructure of composite materials was imaged with a JEOL-200FX transmission electron microscope (TEM). The samples for TEM study were cut into 60–90 nm thick sections with a diamond knife. Surface morphologies of the hydrophobic samples were observed by using SEM (JOEL JSM-7600F). Contact angles (CA) were measured using a First Ten Angstroms FTA 125 goniometer at ambient temperature. Water droplets (about 4 μL) were carefully dropped onto the surfaces of the samples, and the contact angle was determined from the average of five measurements at various positions on the sample surface. The sliding angle (SA) was measured by placing a 4 μL water droplet carefully on the surface, tilting the stage, and recording the angle when the droplet began to move in the downhill direction. The corrosion potential and corrosion current of the sample-coated CRS electrodes were electrochemically measured using a VoltaLab 50 potentiostat/galvanostat. Electrochemical impedance spectroscopy (EIS) measurements were carried out on an AutoLab (PGSTAT302N) potentiostat/galvanostat electrochemical analyzer. Gas permeability (O_2 permeation) experiments were performed using a GTR-31 analyzer (Yangimoto Co., Kyoto, Japan).

2.2 Synthesis and characterization of carboxyl–GNSs

GO derived from SFG44 synthetic graphite powders (TIMCAL®) was synthesized by a modified Hummers method:[36] 4.0 g of synthetic graphite powder and 2.0 g of $NaNO_3$ were put into 280 mL of concentrated H_2SO_4 solution and subsequently stirred for 2 h. Then 16 g of $KMnO_4$ was slowly added into a flask and kept in an ice bath for 2 h. The mixture was diluted with 400 mL of de-ionized water. After that, 5% H_2O_2 was added into the solution until the color of the mixture changed to brown to ensure that $KMnO_4$ was fully reduced. The as-prepared GO slurry was re-dispersed in de-ionized water. Then, the mixture was washed with 0.1 M HCl solution to remove SO_4^{2-} ions. Subsequently, the GO solution was washed with distilled water to remove the residual acid until the solution pH was *ca.* 5 and then vacuum dried at 50 °C. The GO powder was put into the furnace at 1000 °C for 30 s for thermal exfoliation. Finally, we could obtain a few layers of carboxyl–GNSs. The SEM and AFM images of carboxyl–GNSs are shown in Fig. S1 and S2.† The thickness of graphene is about 0.85 nm, which indicates that the graphene is about 2–3 layers. The size of graphene is about 10 μm × 10 μm according to the observation of AFM and SEM images.

Fig. 1 shows the XPS spectra of C 1s of carboxyl–GNSs. The C 1s spectra were normalized by the C=C characteristic peak at 284.5 eV. The C 1s spectra of carboxyl–GNSs show three peaks assigned to oxygen functional groups: C–O from phenol and ether (at 286.1 eV), C=O from carbonyl and quinone (at 287.5 eV), and –COO from carboxyl and ester (at 288.7 eV). The relative intensity of the C–O peak is much larger than those of C=O and –COOH. The carboxylic group content of carboxyl–GNSs was calculated from the XPS spectra using the following equation:[37]

$$\text{Carboxylic group content} = (\text{area}_{C-OH} + \text{area}_{C=O} + \text{area}_{COO})/\text{area}_{total}$$
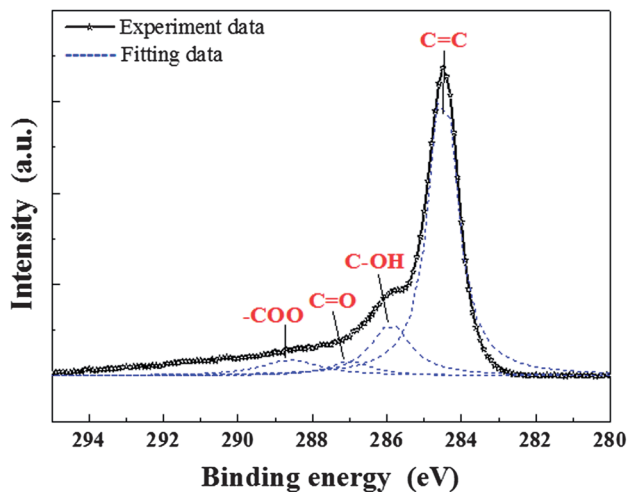
Fig. 1 XPS C 1s spectra of carboxyl–GNSs.

According to the quantitative analysis by Gaussian fitting with three peaks, the contents of C–O, C=O and –COO in carboxyl–GNSs were 11, 5, and 4%, respectively. GNSs were also characterized using X-ray diffraction (XRD) patterns, Raman spectra, and TEM micrographs using similar conditions to those previously reported.[38,39]

2.3 Preparation of PDMS template

The PDMS prepolymer was obtained by mixing the elastomer base and a curing agent in an appropriate ratio (10 : 1, w/w). The PDMS pre-polymer was poured into 3×6 cm^2 molds fixed to a piece of fresh, natural *Xanthosoma sagittifolium* leaf (the veins of the leaf were removed in an area of about 3×6 cm^2) and then cured in a 60 °C oven for 4 h. After curing, the PDMS blocks were separated from the molds and used as templates for imprinting. The thickness of the PDMS template was 3.0 mm.

2.4 UV-curable HPGN coatings

In the imprinting step, drops of the precursor solution were spread on the CRS surface and then the PMDS template was pressed against the precursor solution surface. It was then exposed under UV-light (Fusion UV-curing, light intensity = 2000 mJ cm^{-2}) for 300 s. After the PDMS template was peeled off, the nanocomposite coating with hydrophobic imprinted substrates was obtained.

2.5 Preparation of PGN membranes

The typical procedure for the preparation of PGN membranes with 0.5 wt% of carboxyl–GNSs (denoted PGN0.5) is followed as given: first, 10 g MMA, 0.01 g photo-initiator and 0.05 g carboxyl–GNSs were mixed by magnetic stirring for 12 h at room temperature. After mixing, drops of the mixture solution were spread on the glass plate followed by the UV-curing process. The cured PGN membranes were obtained with a thickness of *ca.* 90 μm.

2.6 Electrochemical corrosion studies

The electrochemical corrosion measurement was performed using a VoltaLab 50. All the electrochemical corrosion measurements were performed in a double-wall jacketed cell, covered with a glass plate, using which water was maintained at a constant operational temperature of 25 ± 0.5 °C. Open-circuit potential (OCP) at the equilibrium state of the system was recorded as the corrosion potential (E_{corr} in mV *versus* saturated calomel electrode (SCE)). Tafel plots were obtained by scanning the potential from −500 to 500 mV above E_{corr} at a scan rate of 10 mV min^{-1}. The corrosion current (I_{corr}) was determined by superimposing a straight line along the linear portion of the cathodic or anodic curve and extrapolating it through E_{corr}. The corrosion rate (R_{corr}, in milli-inches per year, MPY) was calculated from the following equation:

$$R_{corr} \text{ (MPY)} = [0.13 I_{corr}(\text{E.W.})]/[A \times d]$$

where E.W. is the equivalent weight (g per eq.), A is the area (cm^2), and d is the density (g cm^{-3}).

An AutoLab (PGSTAT302N) potentiostat/galvanostat was employed to perform the a.c. impedance spectroscopy measurements. Impedance measurements were carried out in the frequency range of 100 kHz to100 MHz with pure iron (area, 1×1 cm^2) as the working electrode embedded in epoxy, Pt as the counter electrode, and SCE as the reference electrode. The working electrode was first maintained in the test environment for 30 min before the impedance run. All experiments were performed at room temperature. All raw data were repeated at least three times to ensure reproducibility and statistical significance.

3. Results and discussion

Fig. 2 shows the schematic diagram for the fabrication of HPGN coating materials. First, a PDMS prepolymer is cast against a fresh *Xanthosoma sagittifolium* leaf surface and then cured under suitable conditions. The PDMS template prepared has negative *Xanthosoma sagittifolium* leaf surface structures, and is obtained after peeling the leaf off. Second, the substrate is covered with the UV-curable precursor solution, and the
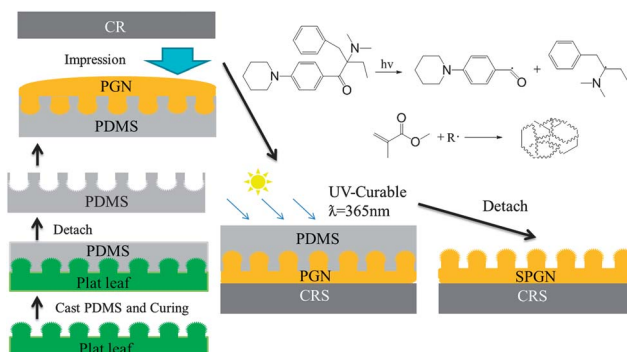

Fig. 2 Preparation process for the superhydrophobic surfaces of nanocomposites using the nanocasting technique.

template is pressed against the CRS. After the UV-curing process and peeling off the PDMS template, a *Xanthosoma sagittifolium* leaf-like surface is formed on the CRS.

3.1 Characterization of PMMA and PGN materials

The representative FTIR absorption spectra of carboxyl–GNSs, PMMA and PGN0.5 are shown in Fig. 3. In the spectra of PMMA and PGN0.5, the characteristic absorbance bands occur in the following assignment: C–H stretching 2949 cm^{-1}, C=O stretching 1723 cm^{-1} and C–O stretching 1447 cm^{-1} reveal the characteristic bands from PMMA. Moreover, on comparing the two curves, no obviously different absorption peak is observed, which is most likely due to the low amounts of graphene.

3.2 Morphology of PGN materials

The morphological studies for the dispersion capability of GNSs can be carried out by observation under a TEM. Fig. 4 shows the micrographs of PGN0.5 taken at 200k magnification on a 120 kV TEM instrument. The bright regions of the photograph at high magnification represent the domain of the PMMA matrix and the dark lines correspond to the cross-section of the layers of GNSs. As shown in Fig. 4, PGN0.5 exhibited relatively well-dispersed GNSs in the PMMA matrix. This indicates that the attachment of carboxylic groups onto the graphene surface could effectively enhance the compatibility between the carboxyl–GNSs and the PMMA matrix, leading to an improvement in the dispersion capability. In addition, the better

dispersion can also be attributed to the formation of hydrogen bonds between the remaining hydroxyl groups of carboxyl–GNSs and the carbonyl group of PMMA.[40]

3.3 Microscopic observations

A photograph of natural, fresh *Xanthosoma sagittifolium* leaves is shown in Fig. 5(a). Fig. 5(b) is the high magnification SEM image of the *Xanthosoma sagittifolium* leaf. The average contact angle on the fresh *Xanthosoma sagittifolium* leaves is *ca.* 146°, as shown in Fig. 5(b). In Fig. 5(b), many small papillary hills are clearly visible on the natural *Xanthosoma sagittifolium* leaf. The diameters of the small papillary hills are between 7 and 9 μm. Fig. 5(c) is the SEM image of the PDMS template prepared by casting the liquid PDMS directly onto a natural, fresh *Xanthosoma sagittifolium* leaf. Many holes whose diameters range from 7 to 9 μm are shown on the surface of the PDMS template. Fig. 5(c) shows the topographic structure of the hole on the surface that complements the papillary hills on the natural, fresh *Xanthosoma sagittifolium* leaf. This result demonstrates that the template effectively replicated the topologically inverse structures of the *Xanthosoma sagittifolium* leaf surfaces.

Fig. 6 shows the structures on the surfaces of the nanocast layers on the CRS slides observed using SEM. Numerous
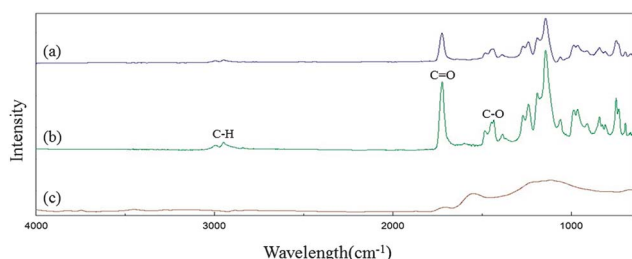

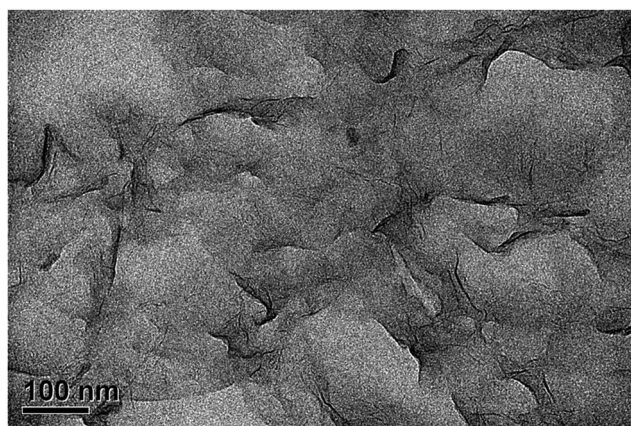**Fig. 3** FTIR spectra of (a) PMMA, (b) PGN0.5 and (c) carboxyl–GNSs.

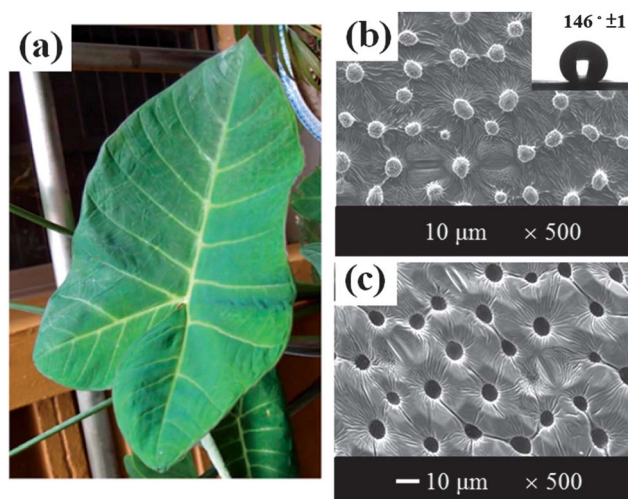
Fig. 4 TEM micrographs of PGN0.5.

Fig. 5 (a) Photograph of the *Xanthosoma sagittifolium* leaves. (b) SEM image of the fresh natural leaf. Illustration is the water contact angle of the *Xanthosoma sagittifolium* leaf. (c) PDMS negative template.
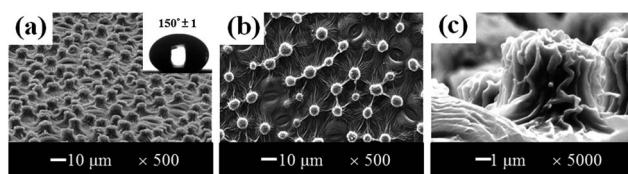

Fig. 6 SEM images of (a) the *Xanthosoma sagittifolium* leaf-like hydrophobic surface of the nanocomposite. The inset shows the contact angle of the polymeric surface. (b) A top-view of the surface of the nanocomposite. (c) A cross-sectional view of the surface of the nanocomposite.

papillary microstructures (*ca.* 7–9 μm average diameter) are formed on the surfaces. The papillary microstructures are replicas of the surface patterns on the *Xanthosoma sagittifolium* leaves.

3.4 Contact angle (wettability) measurements

The coating material replicated from the fresh *Xanthosoma sagittifolium* leaves shows hydrophobic characteristics and a larger water contact angle and smaller slide angle. Fig. 7 shows the change in the water contact angle with various times for HPGN. The durability of the water repellent on the HPGN coating is a very important parameter. The HPGN was stored at room temperature in an ambient atmosphere for one month, and water contact angles were measured hereafter. Almost no decrease in the water contact angle was observed, indicating that the hydrophobic property of the as-prepared HPGN coating is stable enough.

The *Xanthosoma-sagittifolium*-leaf-like-structured PMMA and HPGN coatings obviously have a larger water contact angle and smaller sliding angle (*ca.* 150° and 5°) than the smooth-surface PMMA coating (*ca.* 80° and 60° for contact angle and sliding angle, Table 1). As a significant amount of air was trapped between the papillary hills of the PMMA and HPGN surface, a water drop on such a coating could only make contact with the tops of the papillary hills. Thus, the water placed on the surface of the PMMA and HPGN coatings was likely resting on a thin air cushion.
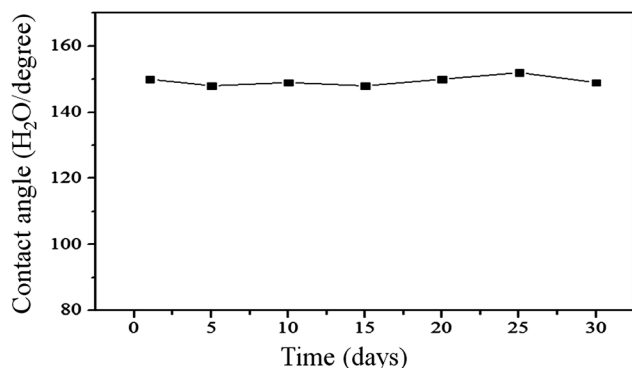

Fig. 7   Change in water contact angle for various times for HPGN.

It should be noted that the topographic structure on the surface of the CRS complements the papillary hills of the natural, fresh *Xanthosoma sagittifolium* leaf. When various smooth substrates such as glass slides or CRS substrates are used, the resulting surface features are almost identical because they are replicated on a thin layer that completely covers the substrate surfaces. The PDMS template played a key role in replicating highly accurate surface features. Because of its low surface energy and good solidification, the PDMS template could be used to replicate the nanostructures on the surface of the *Xanthosoma sagittifolium* leaf with high fidelity and could be easily peeled off without significantly damaging the surfaces. During the process, the template remained in close contact with the substrate under pressure, generating solid nanostructures after replication.

The ability of a coating to protect metal substrates against corrosion depends on three aspects: (1) sorption of water onto the coating, (2) transport of water throughout the coating, and (3) accessibility of water to the coating/substrate interface. Therefore, it is reasonable to accept that the low-wettability HPGN effectively prevented the water from adsorbing onto the substrate surface and therefore exhibited an excellent corrosion resistance in wet environments.

3.5 Potentiodynamic measurements

On the basis of a series of electrochemical measurements (*i.e.*, corrosion potential, polarization resistance, and corrosion current measured in a corrosive medium (3.5 wt% aqueous NaCl electrolyte)), we concluded that the HPGN coating was superior at protecting the CRS electrode against corrosion than the common HP and PMMA coatings. Information about corrosion current can be obtained by extrapolating Tafel plots, from both the cathodic and anodic polarization curves for the respective corrosion processes.[41,42] Extrapolating the cathodic and anodic polarization curves to their point of intersection provides both the corrosion potential and the corrosion current. Corrosion protection studies were performed on samples with 10 ± 1 μm thick coatings and immersed in a corrosive medium for 30 min. Tafel plots for the two samples immersed in the corrosive medium are shown in Fig. 8 and the corresponding data are listed in Table 1.

Table 1   Contact angle, slide angle and electrochemical corrosion measurements of bare CRS, PMMA, HP and HPGN coated electrodes, and gas permeability, moisture absorption of HP and HPGN

Sample code	Electrochemical corrosion measurements[a]					Thickness (μm)	Contact angle (°/H₂O)	Slide angle (°/H₂O)	O₂ permeability (barrier)	Vapor permeability (g m⁻² h⁻¹)	Moisture absorption[b] (%)
	E_{corr} (mV *vs.* SCE)	R_p (kΩ cm²)	I_{corr} (μA cm⁻²)	R_{corr} (MPY)	P_{EF}%						
CRS	−880	0.30	73.40	68.32	—	—	—	—	—	—	—
PMMA	−647	2.84	10.15	9.45	89.44	9 ± 1	80 ± 1	>60	—	—	—
HP	−500	26.52	1.24	1.15	98.87	9 ± 1	149 ± 1	6 ± 0.2	2.70	176	23.5
HPGN	−344	93.63	0.37	0.34	99.68	10 ± 1	150 ± 1	5 ± 0.4	0.81	68	11.9

[a] Saturated calomel electrode (SCE) was employed as a reference electrode. [b] Measured at ambient temperature for 2 days.
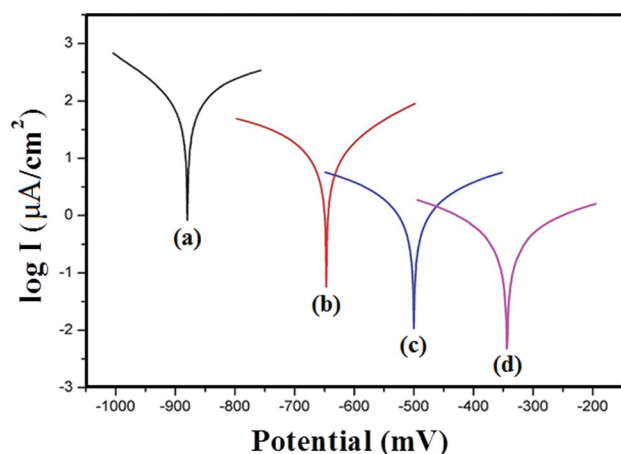
Fig. 8   Tafel plots for (a) bare, (b) PMMA-coated, (c) HP-coated, and (d) HPGN-coated CRS electrodes measured at 25 ± 0.5 °C.

The protection efficiency ($P_{EF}\%$) values were estimated using the following equation:[43]

$$P_{EF}\% = 100[R_p^{-1}(\text{uncoated}) - R_p^{-1}(\text{coated})]/R_p^{-1}(\text{uncoated})$$

where R_p is the polarization resistance (kΩ cm^2), evaluated from the Tafel plots.

The Tafel plots for the sample-coated CRS electrode gave a corrosion potential of $E_{corr} = -647$ and -500 mV for the PMMA and HP coatings, which was more positive than that for the bare CRS electrode, where $E_{corr} = -880$ mV. Moreover, the corrosion current (I_{corr}) of the PMMA and HP-coated CRS electrodes was *ca.* 10.15 and 1.24 μA cm^{-2}, which was significantly lower than that of the bare CRS electrode (*i.e.*, 73.40 μA cm^{-2}).

The corresponding I_{corr} decreased considerably when we used the PGN-coated bare CRS electrode with *Xanthosoma sagittifolium*-leaf-like structures (HPGN) to produce hydrophobic properties. Moreover, the corrosion potential (E_{corr}) of the HPGN-coated CRS electrode was more positive than that of the HP-coated CRS electrode, as E_{corr} increased from -500 to -344 mV (*vs.* SCE) for the HPGN-coated CRS electrode. These electrochemical measurement results show that the HPGN coating provided better protection against corrosion of the CRS electrode than other coatings did.

3.6   Electrochemical impedance measurements

Dielectric spectroscopy, sometimes called impedance spectroscopy or electrochemical impedance spectroscopy (EIS), is used to measure the dielectric properties of a medium and express them as a function of frequency.[44,45] EIS is also used to examine the difference in the activity between the surface of the bare CRS electrode and the HP- or HPGN-coated ones. Impedance is a complex resistance when alternate current flows through a circuit consisting of capacitors, or any of their combination.[46] EIS measurement results in currents over a wide range of frequencies. Complex nonlinear least-squares procedures available in numerous EIS-data-fitting computer programs should be used to fit the model to the experimental

data in order to obtain the Randles circuit parameters. For the simulation studies, corrosion of metals is modeled using an equivalent circuit (called a Randles circuit), as illustrated in Fig. 9, which consists of a double-layer capacitor connected in parallel with a charge-transfer resistor and in series with an electrolyte solution resistor. The impedance (Z) depends on the charge-transfer resistance (R_{ct}), the solution resistance (R_s), the capacitance of the electrical double layer, and the frequency of the AC signal (ω) as follows:

$$Z = Z' + jZ'' = R_s + R_{ct}/[1 + (R_{ct}C_{dl}\omega)^2] + j(R_{ct}{}^2C_{dl}\omega)/[1 + (R_{ct}C_{dl}\omega)^2]$$

The fitting data fit well to all the experimental electrochemical data. The high-frequency intercept is equal to the solution resistance, and the low-frequency intercept is equal to the sum of the solution and charge transfer resistances.[47] In general, a higher semicircle diameter (charge transfer resistance) represents a lower corrosion rate.

Fig. 10 shows the Nyquist plots of the four measured samples. The first sample (a) is uncoated CRS. A series of samples denoted as (b), (c) and (d) represent CRS coated by PMMA, HP and HPGN, respectively. The charge transfer resistances of all samples, as determined by subtracting the intersection of the high-frequency end from the low-frequency end of the semicircle arc with the real axis, are 2.7, 85.7, 164 and 792 kΩ cm^2, respectively. EIS Bode plots (impedance *vs.* frequency) of all samples are shown in Fig. 11. EIS Bode plots
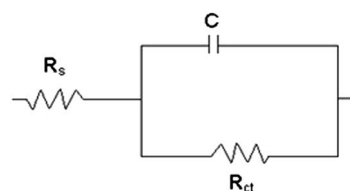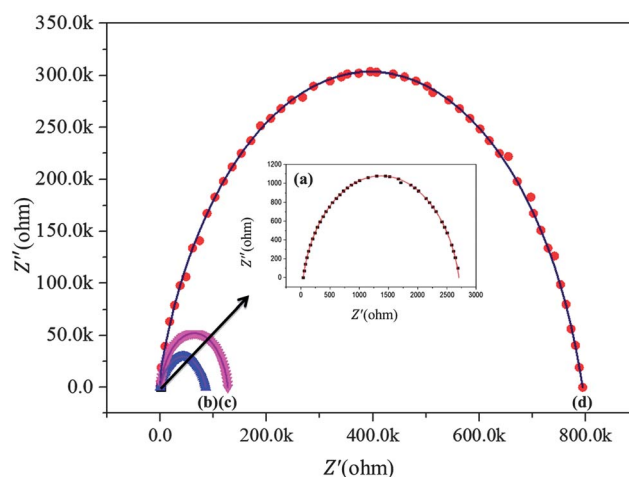

Fig. 9   Randles equivalent circuit.

Fig. 10   Nyquist plot for (a) bare, (b) PMMA-coated, (c) HP-coated, and (d) HPGN-coated CRS electrodes.
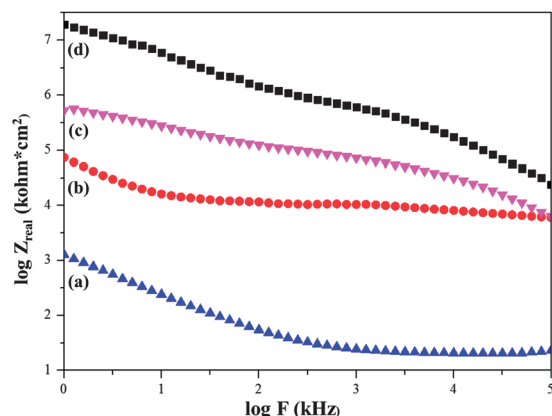
Fig. 11 Bode plot for (a) bare, (b) PMMA-coated, (c) HP-coated, and (d) HPGN-coated CRS electrodes.

(impedance *vs.* frequency) of all samples are shown in Fig. 11. Z_{real} is a measure of corrosion resistance.[48] A low Z_{real} value could be brought about by very high capacitance and/or very low resistance of the coating.[49,50] The large value of the capacitance has been related to the high extent to which water has penetrated the coating.[51] In the case of Bode plots, the value of Z_{real} at the lowest frequency also represents the corrosion resistance. The Bode magnitude plots for uncoated CRS and CRS coated by epoxy, HE, and HEGC show Z_{real} values of 3.1, 4.9, 5.7, and 7.3 kΩ cm^2, respectively, at the low frequency end. These results clearly demonstrate that the HPGN coating protects the CRS electrode against corrosion better than the PMMA and HP coatings. The increase in impedance for the HPGN-coated electrode can be attributed to the hydrophobicity and barrier effects of GNSs dispersed in composites of the coating.

The hydrophobicity and gas barrier effect of HPGN compared to HP and PMMA may result from the low-wettability and dispersed graphene in the PMMA matrix to increase the tortuosity of the oxygen diffusion pathway (lower diffusion length),[52–55] as shown in Fig. 12.
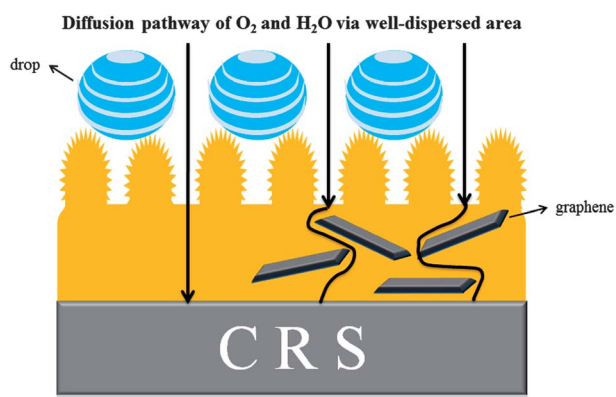

Fig. 12 Schematic representation of the hydrophobic surface and oxygen following a tortuous path through PMMA and PGN materials.

3.7 Molecular barrier and moisture absorption measurements

The membranes of PMMA and PGN materials used for the molecular barrier measurements were prepared with a film thickness of ~90 μm. Compared to PMMA, PGN membranes at 0.5 wt% carboxyl–GNS loading show about 70% and 61% reduction in O_2 and H_2O permeability, as shown in Table 1. The decrease in gas permeability is attributed to the incorporation of the layers of GNSs into the PMMA matrix, which led to a longer tortuosity of the diffusion pathway of oxygen and water vapour.[53,54]

The moisture absorption of PMMA and PGN materials is also shown in Table 1. From the data shown in Table 1, we know that the moisture absorption of PGN was lower than that of PMMA. It is known that a polymer matrix containing more polar groups tends to have higher water absorptive affinity. The nanosheets of graphene tend to reduce the accessibility of the polar groups of PMMA.

4.   Conclusions

In conclusion, a nanocasting technique was used to prepare advanced HPGN coatings for anticorrosion whose surface structure is similar to that of a natural lotus leaf. The morphology of the surface of the as-synthesized HPGN coating showed numerous micro-mastoids, each decorated with many nano-wrinkles. The water contact angle and slide angle of the HP and HPGN coating whose surface was imprinted with the biomimetic pattern of the surface of a natural leaf were about 150° and 5°, which were significantly higher and lower than those of the PMMA coating (*i.e.*, CA = 80°, SA > 60°). From the TEM observations of morphology, relatively well-dispersed GNSs in the PMMA matrix were exhibited. The decrease in gas permeability is attributed to the barrier properties of the layers of GNSs dispersed in the composites. The hydrophobicity and barrier effect of HPGN materials provide them with excellent anticorrosive properties.

Acknowledgements

Notes and references

1 L. Feng, S. Li, Y. Li, H. Li, L. Zhang, J. Zhai, Y. Song, B. Liu, L. Jiang and D. Zhu, *Adv. Mater.*, 2002, **14**, 1857.

2 H. Y. Erbil, A. L. Demirel, Y. Avci and O. Mert, *Science*, 2003, **299**, 1377.

3 T. Sun, L. Feng, X. Gao and L. Jiang, *Acc. Chem. Res.*, 2005, **38**, 644.

4 A. Otten and S. Herminghaus, *Langmuir*, 2004, **20**, 2405.

5 R. Furstner, W. Barthlott, C. Neinhuis and P. Walzel, *Langmuir*, 2005, **21**, 956.

6 T. Liu, Y. Yin, S. Chen, X. Chang and S. Cheng, *Electrochim. Acta*, 2007, **52**, 3709.

7 F. Zhang, L. Zhao, H. Chen, S. Xu, D. G. Evans and X. Duan, *Angew. Chem., Int. Ed.*, 2008, **47**, 2466.

8 F. Zhang, S. Chen, L. Dong, Y. Lei, T. Liu and Y. Yin, *Appl. Surf. Sci.*, 2011, **257**, 2587.

9 A. V. Rao, S. Latthe, S. Mahadik and C. Kappenstein, *Appl. Surf. Sci.*, 2011, **257**, 5772.

10 C. J. Weng, C. H. Chang, C. W. Peng, S. W. Chen, J. M. Yeh, C. L. Hsu and Y. Wei, *Chem. Mater.*, 2011, **23**, 2075.

11 T. I. Yang, C. W. Peng, L. Y. Lin, C. J. Weng, G. Edgington, A. Mylonakis, T. C. Huang, C. H. Hsu, J. M. Yeh and Y. Wei, *J. Mater. Chem.*, 2012, **22**, 15845.

12 A. Taguchi, J. H. Smatt and M. Linden, *Adv. Mater.*, 2003, **15**, 1209.

13 C. Bao, L. Song, C. A. Wilkie, B. Yuan, Y. Guo, Y. Hu and X. Gong, *J. Mater. Chem.*, 2012, **22**, 16399.

14 J. R. Potts, O. Shankar, L. Du and R. S. Ruoff, *Macromolecules*, 2012, **45**, 6045.

15 X. Jiang and L. T. Drzal, *J. Power Sources*, 2012, **218**, 297.

16 M. Li, X. Huang, C. Wu, H. Xu, P. Jiang and T. Tanaka, *J. Mater. Chem.*, 2012, **22**, 23477.

17 B. K. Kim, M. W. Jang, H. C. Park, H. M. Jeong and E. Y. Kim, *J. Polym. Sci., Part A: Polym. Chem.*, 2012, **50**, 1418.

18 Z. Q. Zhu, H. X. Sun, X. J. Qin, L. Jiang, C. J. Pei, L. Wang, Y. Q. Zeng, S. H. Wen, P. Q. La, A. Li and W. Q. Deng, *J. Mater. Chem.*, 2012, **22**, 4811.

19 Z. Q. Zhu, H. X. Sun, G. X. Li, W. D. Liang, X. M. Bao, J. An, P. Q. La, J. F. Dai and A. Li, *J. Appl. Polym. Sci.*, 2013, **129**, 2328.

20 Z. Xu and M. J. Buehler, *ACS Nano*, 2010, **4**, 3869.

21 C. H. Chang, T. C. Huang, C. W. Peng, T. C. Yeh, H. I. Lu, W. I. Hung, C. J. Weng, T. I. Yang and J. M. Yeh, *Carbon*, 2012, **50**, 5044.

22 L. Xu, J. Wang, Y. Song and L. Jiang, *Chem. Mater.*, 2008, **20**, 3554.

23 E. Hermelin, J. Petitjean, J. C. Lacroix, K. I. Chane-Ching, J. Tanguy and P. C. Lacaze, *Chem. Mater.*, 2008, **20**, 4447.

24 M. Qu, G. Zhao, X. Cao and J. Zhang, *Langmuir*, 2008, **24**, 4185.

25 Y. Zhu, J. Li, M. Wan and L. Jiang, *Polymer*, 2008, **49**, 3419.

26 W. H. Ting, C. C. Chen, S. A. Dai, S. Y. Suen, I. K. Yang, Y. L. Liu, F. M. C. Chen and R. J. Jeng, *J. Mater. Chem.*, 2009, **19**, 4819.

27 Y. Lu, H. Cao, S. Zhang and X. Zhang, *J. Mater. Chem.*, 2011, **21**, 8633.

28 C. Li, F. Cheng, J. A. Lv, Y. Zhao, M. Liu, L. Jiang and Y. Yu, *Soft Matter*, 2012, **8**, 3730.

29 Y. Kang, J. Wang, G. Yang, X. Xiong, X. Chen, L. Yu and P. Zhang, *Appl. Surf. Sci.*, 2011, **258**, 1008.

30 A. C. C. de Leon, R. B. Pernites and R. C. Advincula, *ACS Appl. Mater. Interfaces*, 2012, **4**, 3169.

31 X. H. Xu, Z. Z. Zhang, F. Guo, J. Yang and X. T. Zhu, *Appl. Surf. Sci.*, 2011, **257**, 7054.

32 C. W. Peng, K. C. Chang, C. J. Weng, M. C. Lai, C. H. Hsu, S. C. Hsu, S. Y. Li, Y. Wei and J. M. Yeh, *Polym. Chem.*, 2013, **4**, 926.

33 K. C. Chang, H. I. Lu, C. W. Peng, M. C. Lai, S. C. Hsu, M. H. Hsu, Y. K. Tsai, C. H. Chang, W. I. Hung, Y. Wei and J. M. Yeh, *ACS Appl. Mater. Interfaces*, 2013, **5**, 1460.

34 S. C. Sahu, A. K. Samantara, M. Seth, S. Parwaiz, B. P. Singh, P. C. Rath and B. K. Jena, *Electrochem. Commun.*, 2013, **32**, 22.

35 B. P. Singh, B. K. Jena, S. Bhattacharjee and L. Besra, *Surf. Coat. Technol.*, 2013, **232**, 475.

36 W. S. Hummers Jr and R. E. Offerman, *J. Am. Chem. Soc.*, 1958, **80**, 1339.

37 D. Yang, A. Velamakanni, G. Bozoklu, S. Park, S. Meryl, R. D. Piner, S. Stankovich, I. Jung, D. A. Field, C. A. Ventrice Jr and R. S. Ruoff, *Carbon*, 2009, **47**, 145.

38 W. R. Liu, S. L. Kuo, C. Y. Lin, Y. C. Chiu, C. Y. Su, H. C. Wu and C. T. Hsieh, *Open Mater. Sci. J.*, 2011, **5**, 236.

39 S. L. Kuo, W. R. Liu, C. P. Kuo, N. L. Wu and H. C. Wu, *J. Power Sources*, 2013, **244**, 552.

40 V. H. Pham, T. T. Dang, S. H. Hur, E. J. Kim and J. S. Chung, *ACS Appl. Mater. Interfaces*, 2012, **4**, 2630.

41 A. Mitra, Z. B. Wang, T. G. Cao, H. T. Wang, L. M. Huang and Y. S. Yan, *J. Electrochem. Soc.*, 2002, **149**, B472.

42 D. E. Beving, A. M. P. McDonnell, W. S. Yang and Y. S. Yan, *J. Electrochem. Soc.*, 2006, **153**, B325.

43 J. Bockris and K. N. Reddy, *Modern Electrochemistry*, New York, 1976, p. 622.

44 Y. D. Liu, F. F. Fang and H. J. Choi, *Langmuir*, 2010, **26**, 12849.

45 Y. D. Liu, B. J. Park, Y. H. Kim and H. J. Choi, *J. Mater. Chem.*, 2011, **21**, 17396.

46 S. M. Park and J. S. Yoo, *Anal. Chem.*, 2003, **75**, 455A.

47 A. Amirudin and D. Thierry, *Prog. Org. Coat.*, 1995, **26**, 1.

48 F. Zucchi, V. Grassi, A. Frignani, C. Monticelli and G. Trabanelli, *J. Appl. Electrochem.*, 2006, **36**, 195.

49 M. B. Kannan, D. Gomes, W. Dietzel and V. Abetz, *Surf. Coat. Technol.*, 2008, **202**, 4598.

50 A. S. Hamdy, E. El-Shenawy and T. El-Bitar, *Int. J. Electrochem. Sci.*, 2006, **1**, 171.

51 G. Reinhard and U. Rammelt, *Prog. Org. Coat.*, 1992, **21**, 205.

52 I. H. Tseng, Y. F. Liao, J. C. Chiang and M. H. Tsai, *Mater. Chem. Phys.*, 2012, **136**, 247.

53 J. R. Potts, D. R. Dreyer, C. W. Bielawski and R. S. Ruoff, *Polymer*, 2011, **52**, 5.

54 S. Morimune, T. Nishino and T. Goto, *ACS Appl. Mater. Interfaces*, 2012, **4**, 3596.

55 S. S. Ray and M. Okamoto, *Prog. Polym. Sci.*, 2003, **28**, 1539.